

1 First Demonstration of a Pixelated Charge Readout for
2 Single-Phase Liquid Argon Time Projection Chambers

3 J. Asaadi³, M. Auger¹, A. Ereditato¹, D. Goeldi^{*1}, R. Hänni¹, U. Kose², I Kreslo¹,
4 D. Lorca¹, M. Luethi¹, C. Rudolf von Rohr¹, J. R. Sinclair^{†1}, F. Stocker^{1,2},
5 C. Tognina¹ and M. Weber¹

6 ¹Albert Einstein Center for Fundamental Physics, Laboratory for High Energy
7 Physics, University of Bern, 3012 Bern, Switzerland

8 ²CERN, 1211 Geneva, Switzerland

9 ³Department of Physics, The University of Texas at Arlington, Arlington, Texas
10 76019, USA

11 8th January 2020

12 **Abstract**

13 Traditional charge readout technologies of single-phase Liquid Argon Time projection
14 Chambers (LArTPCs) introduce intrinsic ambiguities in event reconstruction, combined with
15 a slow detector response, these ambiguities have limited the performance of LArTPCs, until
16 now. Here, we present a novel pixelated charge readout that enables the full 3D tracking
17 capabilities of LArTPCs. We characterise the signal to noise ratio of charge readout chain,
18 to be about 14, and demonstrate track reconstruction on 3D space points produced by the
19 pixel readout. This pixelated charge readout makes LArTPCs a viable option for the high
20 multiplicity environments.

21 **1 Introduction**

22 Since their evolution from gaseous TPCs [1–3], the charge readout for Liquid Argon Time Projection
23 Chambers (LArTPCs) has been achieved with two or more projective wire planes. Projective wire
24 readouts have been successfully demonstrated in a number of experiments [4–6], however they
25 introduce intrinsic ambiguities in event reconstruction [7]. The ambiguities are due to reconstructing
26 complex 3D shapes with a limited number of 2D projections, and are particularly problematic if
27 tracks are aligned parallel to the wire plane, or multiple events overlap in drift direction. LArTPCs
28 are also slow detectors with a drift speed of $2.1 \text{ mm } \mu\text{s}^{-1}$ at 1 kV cm^{-1} [8], making event pile-up a
29 problem for projective wire readouts in high-multiplicity environments. It is possible to increase
30 drift fields beyond 1 kV cm^{-1} [9, 10], however it is both safer and simpler to overcome pile-up with
31 a charge readout free from ambiguities. For this reason, we have developed a novel approach based
32 on a pixelated charge readout to exploit the full 3D potential of LArTPCs.

33 Pixelated charge readout is not a new idea, it has been employed in gaseous TPCs since the
34 early 2000’s [11]. However, gaseous TPCs are less sensitive to power dissipation from readout
35 electronics than single-phase LArTPCs¹. It is only relatively recently that cold readout electronics
36 became available for LArTPCs [13], with cold preamplifiers designed specifically for wire readouts.
37 Existing wire readout electronics however cannot be applied to such a scheme due to the increase
38 in channel number. Ideally, the charge collected at every pixel would be amplified and digitised
39 individually. To make use of existing cold wire readout electronics for the measurements described
40 here, a form of analogue multiplexing had to be employed. While not ideal, this allowed for the

*Corresponding author: goeldi@protonmail.com

†Corresponding author: james.sinclair@lhep.unibe.ch

¹Charge readout in dual-phase LArTPCs is not constrained by power dissipation, so they are able to exploit more advanced schemes [12].

41 proof of principle of a pixelated charge readout in a single-phase LArTPC. Bespoke pixel readout
42 electronics are being developed [14] as a result of our work.

43 LArTPCs are ideal neutrino detectors due to their high density, homogeneous calorimetry, and
44 the potential for precise 3D tracking. Hence, LArTPCs have been selected as the far detector for the
45 future long-baseline Deep Underground Neutrino Experiment (DUNE) [15]. DUNE faces increasing
46 sensitivity demands that will be met by high statistics and improved background rejection. To
47 increase statistics at the far detector site, 1300 km from the target, a neutrino beam $\mathcal{O}(1 \text{ MW})$
48 is required. At the near detector, only 574 m from the target, this beam intensity corresponds
49 to $\mathcal{O}(0.1)$ events per tonne per beam spill [16, 17]. To minimise detector response uncertainties
50 between the near and far, it would be ideal to have a LArTPC component of the DUNE near
51 detector complex. A pixelated charge readout would make LArTPCs suitable for near detector
52 environments.

53 In this paper we demonstrate the primary goal of a pixelated charge readout, direct access to
54 3D space points for event reconstruction, and the characterisation of the Signal to Noise Ratio
55 (SNR) of such a readout.

56 2 Experimental Set-up

57 2.1 Pixel PCB Design

58 The pixelated anode plane used in our tests, shown in Figure 1, was produced as a conventional
59 eight-layer Printed Circuit Board (PCB). The pixelated area is 100 mm across, with pixels formed of
60 900 μm diameter vias (PCB interlayer connections) with a pitch of 2.54 mm. An inductive focusing
61 grid surrounds the pixels, it is made from 152.4 μm wide copper traces split into 28 regions. There
62 are 6 \times 6 pixels per region, giving a total of 1008 pixels.

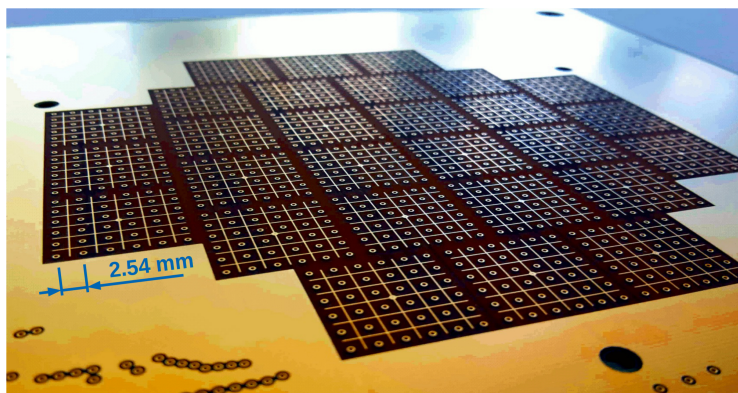


Figure 1: Initial (July 2016) prototype pixelated anode PCB. The pixelated readout area is 100 mm in diameter. Each charge collection pixel is a 900 μm via, at a pitch of 2.54 mm, inductive focusing grids formed of 152.4 μm copper traces surround the pixels. There are 28 inductive focusing grids with 36 pixels per region, a total of 1008 pixels.

63 Vias were used for pixels instead of pads in order to minimise capacitance. It is important
64 that capacitance is minimised when amplifying charge since thermal noise scales with capacitance:
65 $Q_{\text{Noise}} = \sqrt{k_B T C}$ [18]. To further minimise parasitic capacitance, the PCB design was optimised
66 by removing unnecessary ground planes, routing signal tracks outside necessary ground planes, and
67 increasing the thickness of the PCB to 3.5 mm from an initial 1.75 mm. Capacitance at each pixels
68 is $\mathcal{O}(50 \text{ pF})$, however a significant contribution to this is due to additional traces required for the
69 multiplexing scheme.

70 As shown in Figure 2, the pixels are directly coupled to the preamplifiers. The inductive focusing
71 grids are coupled to the preamplifiers via a 10 nF capacitor, and are connected to the bias voltage
72 via a 10 M Ω resistor and an RC filter. The RC filter consists of another 10 M Ω resistor and a 10 nF
73 capacitor to ground.

74 The bias on the inductive focusing grids had to be sufficient to allow full charge transparency
75 (all charge collected by the pixels), yet low enough to minimise any risk of damaging the cold
76 coupling capacitors.

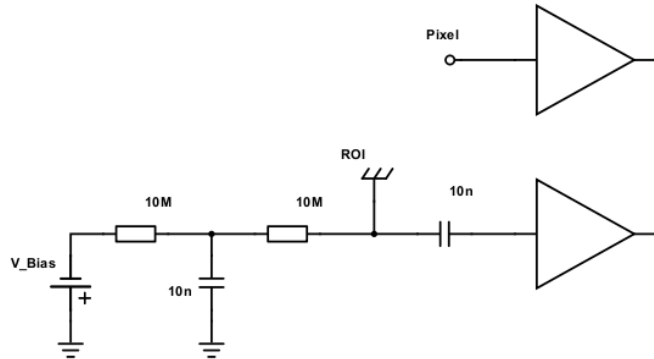


Figure 2: Circuit diagram for pixel and inductive focusing grid (ROI). Pixels are directly coupled to the preamplifiers. ROIs are coupled to the preamplifiers via a 10nF capacitor, and are connected to the bias voltage via a $10\text{ M}\Omega$ resistor and an RC filter. The RC filter consists of another $10\text{ M}\Omega$ resistor and a 10nF capacitor to ground.

2.2 Readout Scheme

Cryogenic preamplifiers were used to minimise both the noise-sensitive unamplified signal path and the thermal noise introduced by the amplifier itself [19]. The preamplifier Application Specific Integrated Circuits (ASICs) used are the LARASIC4* [13] designed by the Brookhaven National Lab, first tested in the ARGONTUBE experiment [19] and deployed in the MicroBooNE and LArIAT experiments [6, 20]. LARASIC4*s were designed for traditional wire readouts, which require fewer channels than a pixelated readout of equivalent dimensions. Therefore, no focus was placed on high channel density, and the LARASIC4*s have only 16 channels per chip. Given the 1008 pixels, cold digitisation is disfavoured due to power consumption constraints. Ideally, every pixel would be read out and the signals then digitally multiplexed, requiring bespoke pixel ASIC capable of cold amplification and digitisation for many channels. Such ASICs are being developed by Lawrence Berkeley National Lab [14], as a result of this work. Therefore, analogue multiplexing had to be used to minimise the channel numbers, with signals digitised at room temperature outside the cryostat.

The multiplexing scheme [21] divides the pixels into a number of Regions Of Interest (ROIs). Each ROI is defined as the pixels contained within a single inductive focusing grid. All pixels at the same coordinate inside each of the ROIs are connected to the same DAQ channel, i.e. only one DAQ channel connects all the pixels in the top left corners of all ROIs, and so on. For a general expression of the multiplexing scheme, a pixel plane of $N \times N$ pixels (where $N = n^2$ and n integer) is divided into $n \times n$ ROIs, each ROI containing, again, $n \times n = N$ pixels. Reading out such a plane requires N DAQ channels for the ROIs plus another N channels for the pixels. With the employed multiplexing scheme, only as many pixel channels as there are pixels per ROI are required, due to the fact that all pixels at the same relative position across all ROIs share a common DAQ channel. This means that an $N \times N$ pixel plane requires only $2N$ DAQ channels; the same as a conventional 2-plane wire readout of the same pitch, and dimension. Optimising the number of ROIs allowed us to readout the 1008 physical pixels with only 64 DAQ channels (28 ROIs + 36 pixels).

Pixel signals are then associated to an induction signal on the ROI grid as follows. If there is a signal on a certain pixel DAQ channel, the position inside the ROI is known but not which ROI. By combining the inductive bipolar pulse on the ROI grid with any simultaneous collection pulses from the pixels, it is possible to disentangle the true position. Again, the drawback of this approach is that it is not free from ambiguities; it fails for multiple simultaneous hits when it is impossible to say which pixel pulse belongs to which ROI pulse. Ambiguous hits are flagged as pixel signals corresponding to multiple ROI signals, which can be disentangled later using reconstruction tools.

2.3 Pixel Demonstration TPC

The pixel demonstration TPC, shown in Figures 3 and 4, is cylindrical with an inner diameter of 101 mm and a 590 mm drift length. The TPC operated with a drift field of 1kV cm^{-1} , corresponding

113 to a total drift time of 281 μ s. The field-cage consists of aluminium rings supported by clear acrylic
 114 rings, with a cathode formed of a brass disc. The dimensions of the field-cage and cathode are
 115 shown in Figure 3. Alternating acrylic rings are split, to allow for the circulation of purified LAr
 116 within the TPC volume. Four square section PAI² uprights support the cathode and field cage,
 117 with PEEK³ screws fixing the pillars to the acrylic rings. The four PAI uprights connect to a
 118 PAI frame which supports the anode plane and a set of Silicon PhotoMultipliers (SiPMs) for light
 119 readout, see Figure 4.

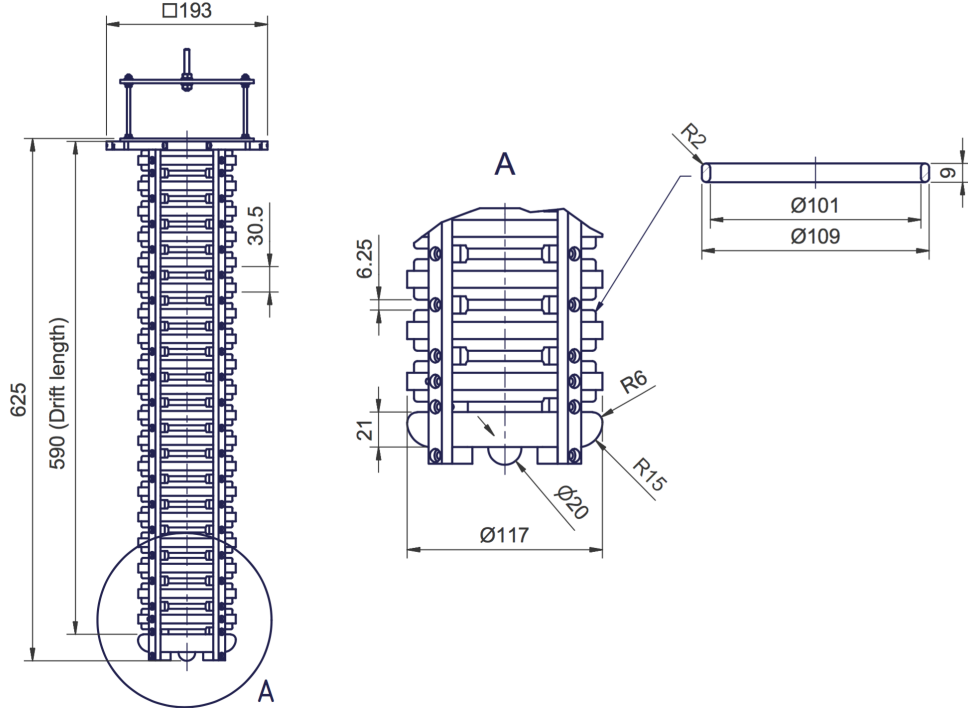


Figure 3: Engineering drawing of the pixel demonstration TPC; 590 mm drift length; 6.25 mm field cage spacing; 101 mm internal diameter.

120 The resistive divider consists of a chain of 100 M Ω Vishay Rox metal oxide resistors⁴. Each
 121 resistor is soldered to its neighbour, and fixed to the field cage at each joint with an M3 screw.

122 The acrylic rings provide the light collection; their inner surfaces are machine-polished and
 123 coated with the WaveLength Shifter (WLS) TetraPhenylButadiene (TPB). The coating method is
 124 based on [22]. 0.5 g of TPB and 0.5 g of acrylic flakes were dissolved in 50 mL of toluene and then
 125 mixed with 12 mL of ethanol, which serves to increase the coating homogeneity. Three layers of the
 126 coating were applied by hand, with a fine brush.

127 WLS fibres of 1 mm diameter (Kuraray Y11(200)M) couple the acrylic rings to four SiPMs
 128 (Hamamatsu S12825-050P) mounted close to the anode, see Figure 4. The SiPMs and their front-end
 129 electronics were adapted from those developed at Bern for the cosmic ray taggers used in the
 130 MicroBooNE and SBND experiments [23, 24]. For operation at LAr temperatures, the SiPM bias
 131 voltages had to be reduced from a nominal 70 V at room temperature to 53 V, in order to follow the
 132 drop in breakdown voltage due to temperature. In the front-end electronics, two coincidences
 133 of two out of the four SiPMs are formed and combined by means of a logic *OR* operation. This
 134 coincidence is used in order to improve trigger purity.

135 2.4 Infrastructure

136 The pixel demonstration TPC is housed in a double-bath vacuum-insulated cryostat with the outer
 137 bath open to atmosphere for cooling. The inner LAr is filtered first on filling through a pair of
 138 Oxsorb-Hydrosorb filters, and then recirculated through a single custom-made filter containing

²Polyamide-imide

³Polyether ether ketone

⁴ROX100100MFKE

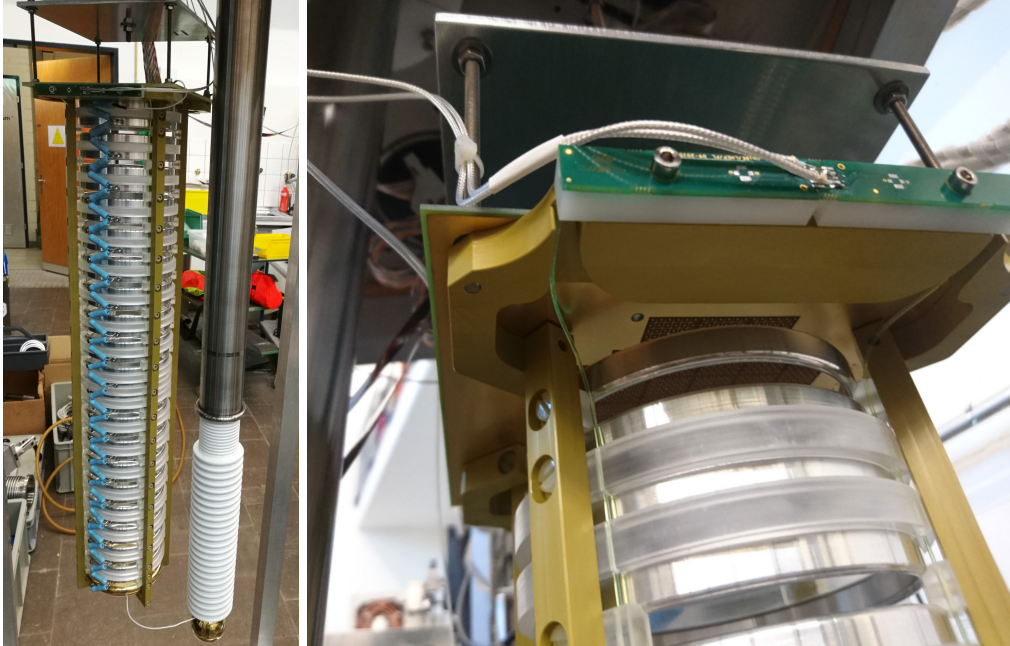


Figure 4: Left: Photograph of the pixel demonstration TPC at Bern, with the HV feedthrough. Right: Close-up of the light collection system, showing wavelength shifting fibres coupling SiPMs to the TPB-coated light guides.

139 both activated copper and silica gel. The cryostat and filtering method were previously used for
 140 LAr purity measurements [25], and High-Voltage (HV) breakdown studies [26]. Based on these
 141 previous studies, an impurity concentration $\mathcal{O}(1 \text{ ppb})$ of oxygen-equivalent is estimated, which
 142 corresponds to a charge lifetime of $290 \mu\text{s}$.

143 The HV feedthrough remains unchanged from the breakdown studies; based on a PET-C
 144 polymer dielectric capable of withstanding potentials as high as -130 kV . A low-pass filter was
 145 added between the power supply and feedthrough, which consists of an 800 pF decoupling capacitor
 146 grounded between two $100 \text{ M}\Omega$ resistors connected in series, all of which is submerged in transformer
 147 oil.

148 Only the warm signal path of the Data Acquisition (DAQ) was altered from that described
 149 in [8], to include differential signalling. An inverted waveform of the signal is put onto an additional
 150 conductor, and the difference is then taken between the signals on the two conductors. Ground
 151 loops are avoided because the signal sink does not need connecting to the same ground as the signal
 152 source. Additionally, the completely symmetric signal path means inductive noise pick-up is equal
 153 on both conductors and therefore cancelled at the signal sink.

154 3 Data Analysis and Reconstruction

155 The primary purpose of this experimental set-up is to demonstrate the principle of 3D reconstruction
 156 utilising a pixelated charge readout within a LArTPC. In this section we focus on both the
 157 characterization of the signal to noise ratio and the basic 3D track reconstruction that is made
 158 directly possible by this technology.

159 For reconstruction, the HV for the TPC was set to -63 kV , which, after a voltage drop across
 160 the HV filter and resistors, corresponds to a 1 kV cm^{-1} drift field. The inductive focusing grid was
 161 set to a bias of -300 V , at which transparency was observed.

162 Both drift field and focusing bias were switched off for the noise measurement since the purpose
 163 is to characterise only the pixel readout, and not the whole TPC.

164 3.1 Signal to noise ratio

To assess the Signal to Noise Ratio (SNR), dedicated noise data was taken employing a 5 Hz random trigger. For the 2000 recorded events, all pixel and ROI channels were combined respectively and

filled into amplitude distribution histograms. The standard deviation of the two noise distributions was then extracted from a Gauss fit. This value was used to calculate the noise for pixel and ROI channels according to

$$\text{SNR} = \frac{S}{\sigma}, \quad (1)$$

where σ is the noise standard deviation from the Gaussian fit and S is the expected signal, which will be explained in detail below. As can be seen in Figure 5a, pixel channel number 10 is significantly noisier in comparison to others, likely caused by a broken preamplifier. Therefore, this channel was blinded for the SNR calculations. The resulting equivalent noise charge is 1095 e for the pixel channels and 982 e for the inductive ROI channels.

The signal S is often taken for a Minimum-Ionising Particle (MIP) as this is a typical low-amplitude signal interesting for neutrino physics. Correctly deriving the deposited charge from experimental data requires a calibrated event reconstruction which was not available at the time of writing. Therefore, we estimated the MIP signal from theory assuming an energy loss of 2.1 MeV cm^{-1} [27]. This can be converted to charge loss using the energy required to produce one electron-ion pair: $W_i = 23.6\text{ eV e}^{-1}$ [28]. Additionally, charge recombination, diffusion and attachment losses characterised by lifetime need to be taken into account. The recombination factor was measured by both ICARUS and ArgoNeuT [29, 30], and found to be $R_c \approx 0.7$ for a drift field of 1 kV cm^{-1} . For a non-zero drift field, diffusion needs to be split into longitudinal and transverse components. Using the ARGONTUBE detector [31], we earlier measured a transverse diffusion coefficient of $D_T = 5.3\text{ cm}^2\text{ s}^{-1}$ at 0.25 kV cm^{-1} while Gushchin et al. [32] report a value of $D_T = 13\text{ cm}^2\text{ s}^{-1}$ at 1 kV cm^{-1} . Even using the more conservative value, this results [33] in a transverse spread of

$$\sigma_T = \sqrt{2D_T t} \approx 0.9\text{ mm}, \quad (2)$$

for our drift time of $t = 281\text{ }\mu\text{s}$; a value well below the pixel pitch of $d_p = 2.54\text{ mm}$. Considering that the longitudinal component is smaller than the transverse [33], we neglect diffusion completely for our calculations. Finally, our lifetime of $290\text{ }\mu\text{s}$ reduces the charge to $\approx 38\%$ over the full drift distance. Combining this, we get a signal of

$$S = \frac{dE}{dx \text{ MIP}} \frac{R_c d_p}{W_i} = 15\,821\text{ e}, \quad (3)$$

for a charge deposited adjacent to the readout plane, and $S = 6004\text{ e}$ for a charge deposited adjacent to the cathode.

Table 1 lists the SNR values obtained from these signal values and the aforementioned measured equivalent noise charge, using Equation (1).

Table 1: SNR values obtained from Equation (1) using the theoretical signal of a MIP at the readout plane or cathode, respectively combined with the average equivalent noise charge for pixel and ROI channels obtained from measurements.

Channel	MIP at	SNR
Pixel	Readout plane	14
Pixel	Cathode	5.5
ROI	Readout plane	16
ROI	Cathode	6.1

174 **3.2 3D track reconstruction**

175 A sample of several thousand cosmic ray events were collected, mostly minimum ionising muons
176 traversing the TPC, to demonstrate 3D track reconstruction. These events were triggered by the
177 light readout described in Section 2.3.

178 The reconstruction procedure comprises five steps:

- 179 1. Noise filtering
180 2. Pulse finding
181 3. 3D hit finding
182 4. Ambiguity rejection
183 5. Track fitting

184 These steps are explained in the following and depicted in Figures 5 through 9, all taken from
185 the same MIP (cosmic muon) event.

186 In the first step, a noise-filtering algorithm is applied to the raw data. As can be seen from
187 Figure 5, the noise is largely correlated across all the channels⁵. This common-mode correlation can
188 be exploited by the noise filter algorithm. The following is done separately for the all pixel and ROI
189 channels of each event. Similarly to the SNR calculation, all samples are filled into an amplitude
190 distribution histogram for each channel, and subsequently fitted with a Gaussian distribution. A
191 noise band is defined per channel with its centre equal to the mean of the Gauss fit and its width
192 equal to the standard deviation multiplied by a tunable scaling factor. The signal amplitudes of
193 all channels within the corresponding noise band are then averaged for each sample. Finally, this
194 average is subtracted from each channel at the corresponding sample. We chose this technique
195 because it effectively suppresses the dominating common mode noise. At the same time, spurious
196 signals produced by high amplitudes from collected charge distorting the average are kept to a
197 minimum by only accepting values within the noise band. The effectiveness of the filtering can be
198 seen in Figure 6, showing the same raw data as Figure 5 post filtering.

199 The second step applies a recursive pulse finding algorithm (pulse finder). The following is
200 performed for each channel independently. Most thresholds employed by the pulse finder are, again,
201 derived from noise levels. Therefore, noise mean and standard deviation are recalculated after noise
202 filtering. A peak threshold is defined by multiplying the noise standard deviation by a tunable
203 scaling factor and adding the noise mean. In the same fashion, an edge threshold lower than the
204 peak threshold is defined to detect the leading and trailing edges of the pulse. Then, the sample
205 with the highest amplitude is found. If it is below the peak threshold, the process stops and proceeds
206 to the next channel. Otherwise, the pulse is scanned in positive and negative directions until it
207 crosses the edge threshold. After this, the whole pulse is stored and deleted from the input data;
208 then the process starts over with finding the new maximum sample and checking it against the
209 peak threshold. For stability reasons, the peak threshold derived from the noise levels is compared
210 against an absolute threshold and the higher of the two is applied. The search is extended to the
211 negative half-pulse for the bipolar ROI pulses, including detection of zero crossing defined by the
212 noise mean. The different thresholds employed and samples found by this process are illustrated in
213 Figure 7.

214 Identified pulses are then combined into 3D hits by matching every pixel pulse to any ROI
215 pulses overlapping in time. In Figure 7, a pixel and ROI pulse are matched if their time slices,
216 defined by the vertical dashed lines, overlap. If a pixel pulse is matched to multiple ROI pulses, an
217 ambiguity occurs, i.e. multiple 3D hit candidates. The employed 3D hit finding results in a rather
218 high amount of ambiguities, but minimises the number of missed hits.

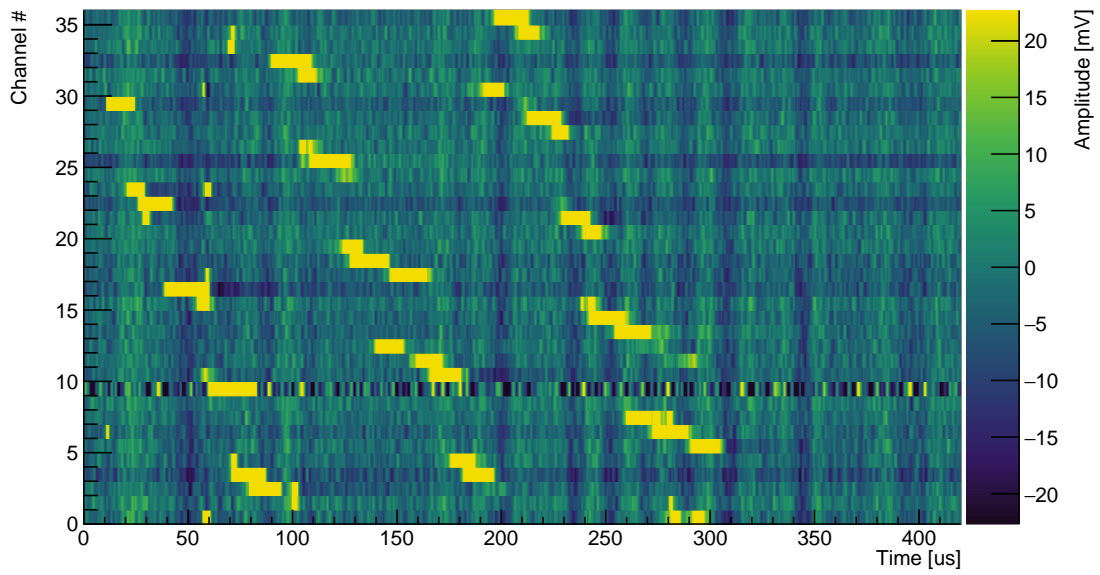
219 To resolve the ambiguities, a Principal Component Analysis (PCA) is applied to the 3D hit
220 candidates in a fourth step. This technique is well established and described in literature, e.g. [34].
221 The basic idea is to calculate three orthogonal eigenvectors of the 3D space point cloud, representing
222 the three axes of an ellipsoid fitted to the data points. In case the points form a track, one of
223 these eigenvectors will have a much higher eigenvalue than the other two. This eigenvector is taken
224 as an estimate for the track direction. We resolve the ambiguities by selecting the hit candidate
225 closest to the track estimate. Furthermore, this procedure can be used to recursively reject outliers
226 by forming a cylinder around the track estimate with a radius proportional to the second largest

⁵Due to the much higher signal levels, the noise is barely visible on the pixel channels in Figure 5a.

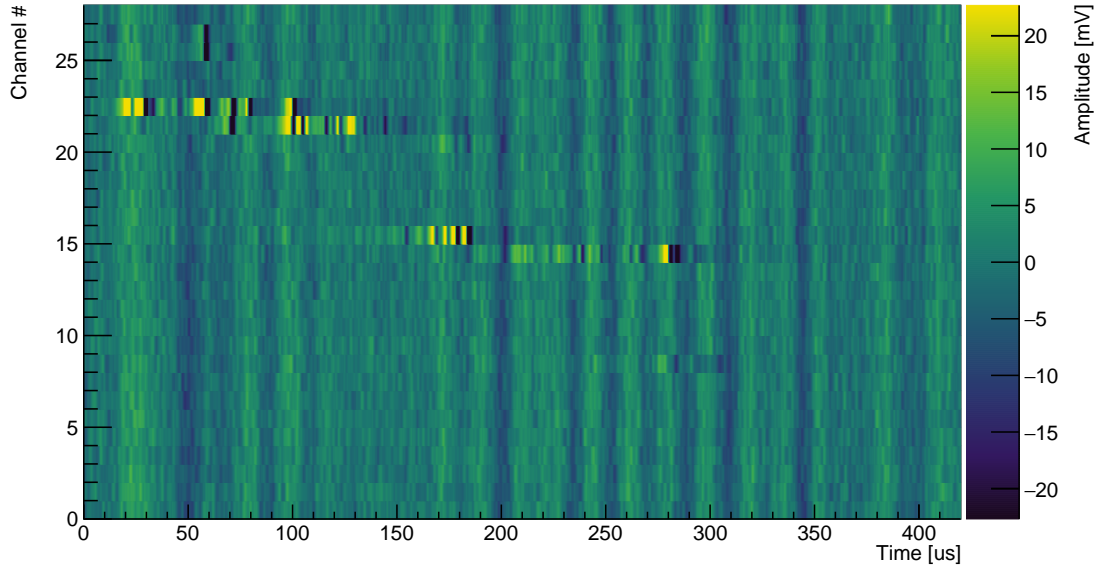
eigenvalue. All hits outside this cylinder are rejected. To reject further outliers the PCA is rerun on the remaining points up to three times, or until either no new outliers are rejected, or 40 % of the hit candidates have been rejected. In a later stage of reconstructing more complex events, this algorithm can potentially be used to cluster 3D hits in order to separate multiple tracks. The PCA ambiguity rejection is illustrated in Figure 8. It should be noted that this step will not be required if the ROI-multiplexing scheme can be avoided, e.g. using cold electronics capable of digitising every single pixel in situ.

The final step consists of a Kalman filter for track identification. For this, we used the well-established GENFIT track fitting package [35, 36]. Ionisation losses and multiple scattering are taken into account. While generally applicable to any particle type, as a proof of concept we assumed a minimum-ionising muon with an initial momentum of 260 MeV in the direction of the track estimate from the PCA. To deal with potential outliers still remaining after the PCA, we chose a recursive algorithm, a so-called *deterministic annealing filter*. It works by assigning successively lower weights to outliers with each recursion step. For more details we refer to the respective publications [35, 36]. The resulting track is shown in Figure 9.

In the near future, the Kalman filter will be capable of fitting the particle momentum and/or even particle type to the data. However, at the time of this writing, this was not implemented. In particular, the momentum stays roughly at the initial guess of 260 MeV. A potential explanation for this is that the resolution of our detector is too low to estimate momentum from multiple scattering. Another explanation might be the hit finder missing hits due to non-optimal tuning. Proper tuning of the reconstruction requires a full simulation chain of the detector which is not yet available. Using data to tune the reconstruction is prone to the introduction of circular biases. On the other hand, most of the difficulties emerge from the multiplexing ambiguities and their resolution. While the presented 3D readout already reduces the reconstruction complexity compared to a classical wire readout, an ambiguity-free readout will make reconstruction even easier by completely eliminating the need to resolve ambiguities.

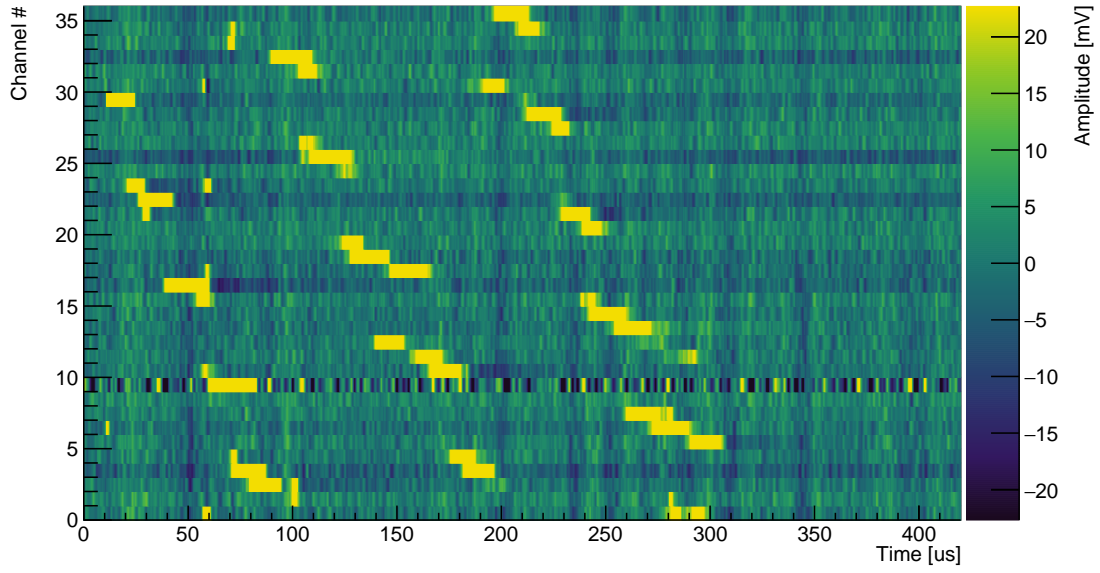


(a) Pixel raw data

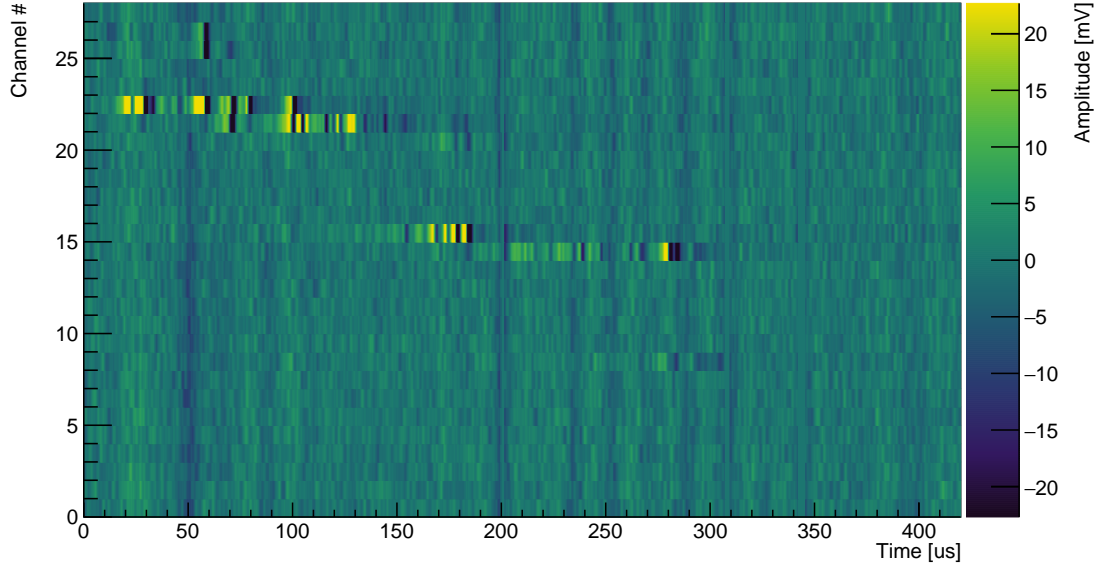


(b) ROI raw data

Figure 5: Unfiltered raw data of a typical MIP event (the same event as in Figures 6 through 9). Note that the colour scale was adjusted to highlight the charge signals. Therefore, most signal peaks are above/below the maximum/minimum of the colour scale. The full range of a typical signal can be seen in Figure 7.

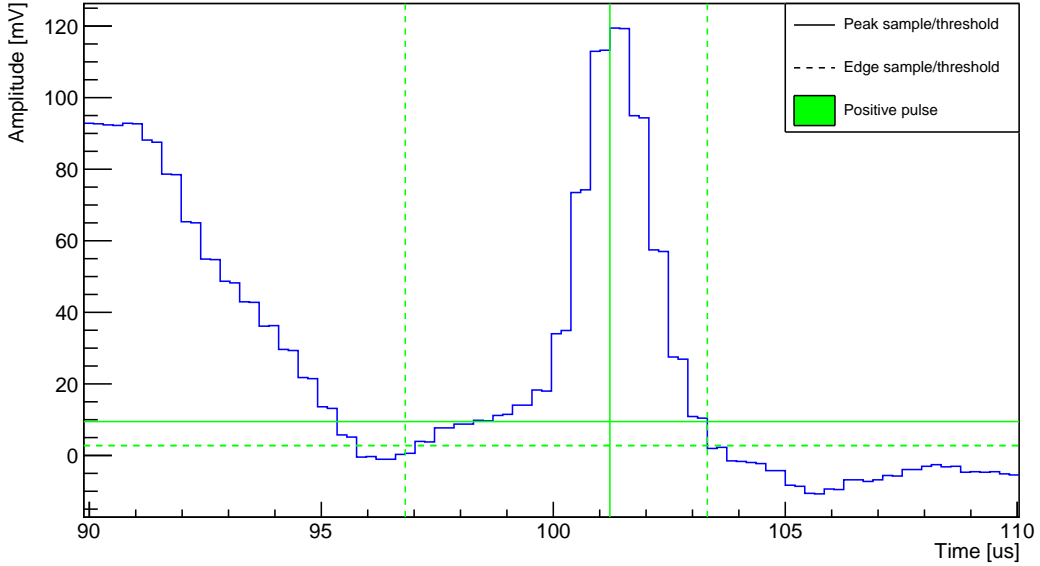


(a) Pixel raw data

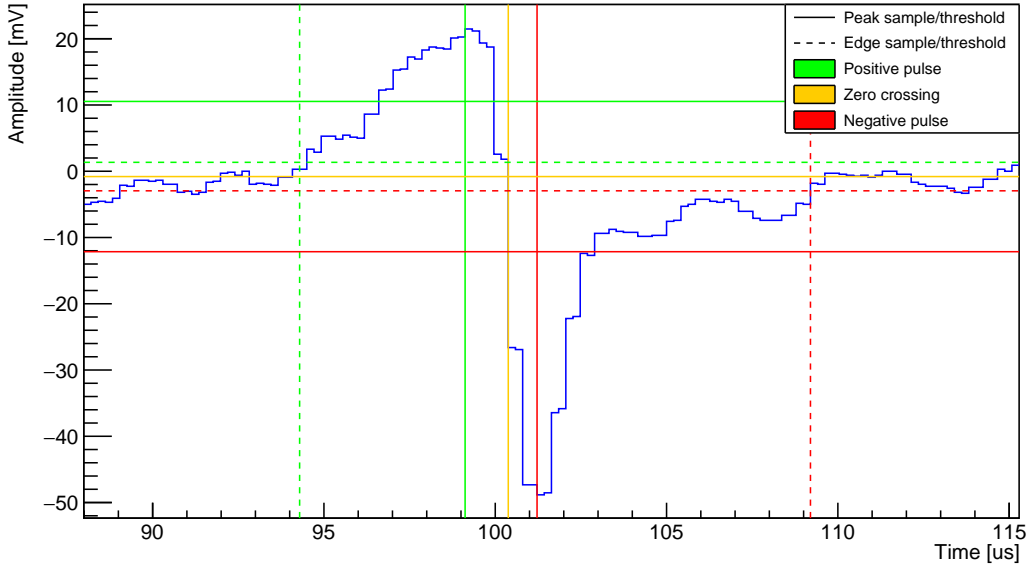


(b) ROI raw data

Figure 6: Filtered data of a typical MIP event (the same event as in Figures 5, and 7 through 9). Note that the colour scale was adjusted to highlight the charge signals (same scale as in Figure 5). Therefore, most signal peaks are above/below the maximum/minimum of the colour scale. The full range of a typical signal can be seen in Figure 7.

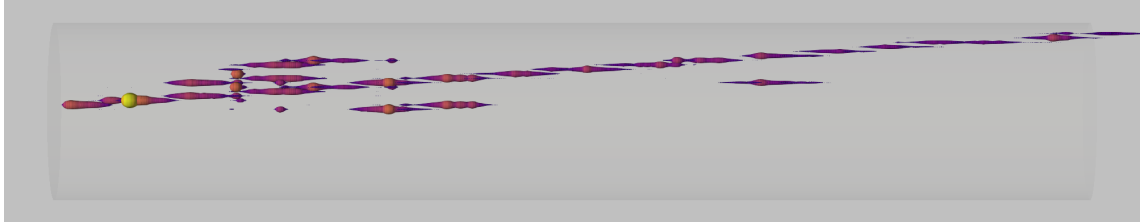


(a) Pixel pulse

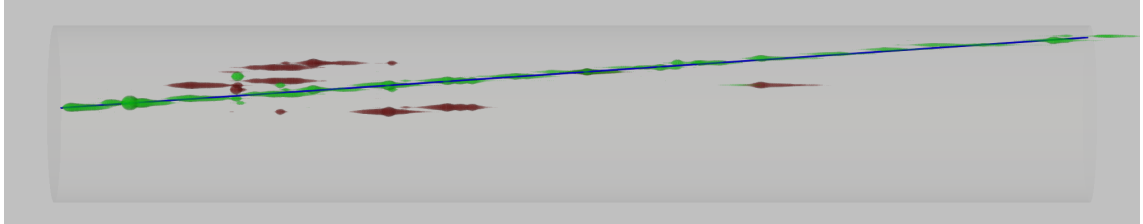


(b) ROI pulse

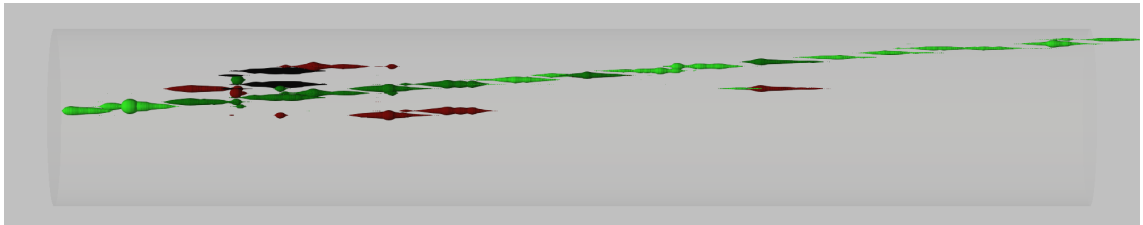
Figure 7: Pulse shapes of a single hit of a typical MIP event (the same event as in Figures 5, 6, 8, and 9). Superimposed are the thresholds of the pulse finding algorithm. Horizontal lines represent thresholds: solid are the minimum thresholds required to be crossed for a pulse to be detected, and dashed are the thresholds used to detect the pulse edges. Vertical lines represent the corresponding detected peak/edge samples. Colour indicates a positive (green) or negative (red) pulse, or a zero crossing (yellow). Note that the yellow zero-crossing threshold is not exactly zero as it is defined by the mean of the noise.



(a) Colour-coded amount of collected charge



(b) Ambiguity resolution employing a principal component analysis: Green hits are accepted while dark red ones are rejected. This is achieved by selecting the ambiguity closest to the eigenvector of the point cloud with the largest eigenvalue, represented by the blue line.



(c) Colour-coded degree of ambiguity: Light green are unambiguous hits while dark green are selected solutions of ambiguous hits. Dark red through black are rejected solutions of ambiguous hits where darker colour represents a higher degree of ambiguity. As this is a quite clean track with only few short δ rays, there are no outliers rejected other than the multiplexing ambiguities.

Figure 8: Reconstructed 3D hits from the hit finder. Axes are the same as in Figure 9. The passing particle is most likely a cosmic μ entering from the left (the same event as in Figures 5 through 7, and 9). Drift direction is from right to left. Each hit is represented by a sphere of a radius proportional to the pulse height. This results in a droplet shape because the radius decreases when the ionisation track moves towards a neighbouring pixel, depositing less charge on the current pixel over time.

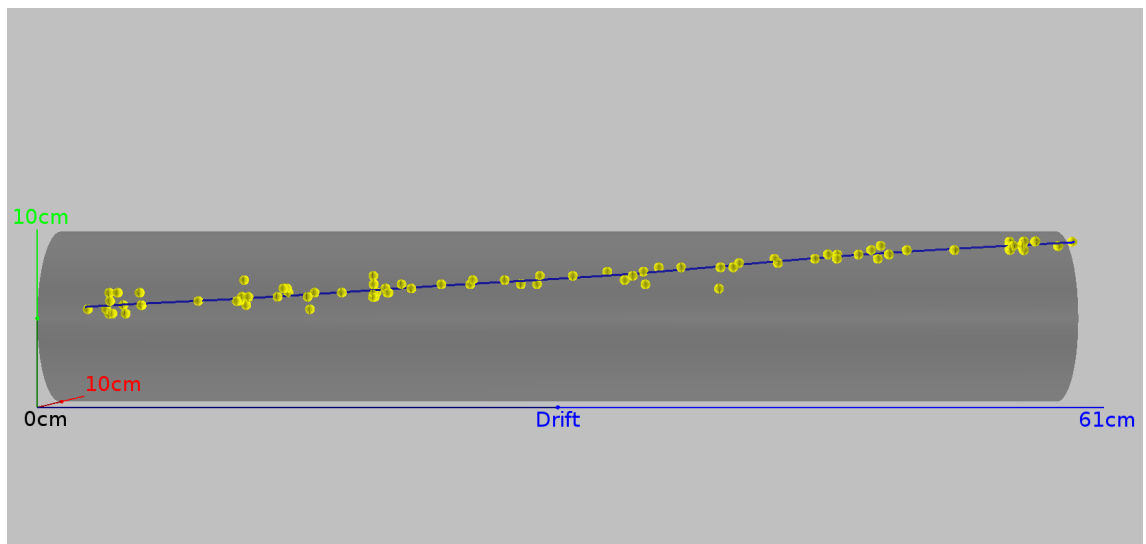


Figure 9: Track fitted by the Kalman filter. The TPC volume is shown in faint grey. The passing particle is most likely a cosmic μ entering from the left (the same event as in Figures 5 through 8). Drift direction is from right to left. The yellow points are the input to the Kalman filter, the accepted hits from the principal components analysis. Blue is the output, a fitted track taking into account ionisation losses and multiple scattering in LAr.

253 4 Conclusions

254 We have presented a proof of concept for a pixelated charge readout for single-phase LArTPCs
255 by successfully building and operating a pixelated LArTPC, and reconstructed 3D tracks of
256 cosmic muons crossing the TPC. The requirement of high readout channel number has not yet been
257 addressed. In this first implementation, we have used existing wire readout electronics in conjunction
258 with analogue multiplexing which introduces ambiguities. Although much improved compared to
259 classical wire readouts, the signal to noise ratio of and the multiplexing ambiguities complicated
260 reconstruction. This work shows that it is of paramount importance to be capable of digitising
261 the charge signals at cryogenic temperatures allowing for digital multiplexing and thus enabling a
262 true, ambiguity-free, 3D LArTPC charge readout. Work is currently under way to develop bespoke
263 pixel readout electronics, based on the requirements highlighted by this demonstration. Once
264 this last remaining problem is solved, pixelated charge readouts will enable the true 3D tracking
265 capabilities of single-phase LArTPCs. This work has been a success in reconstructing the first
266 particle track in a LArTPC using a pixelated charge readout. This technology will provide the
267 necessary reconstruction efficiency and background rejection to enable LArTPCs to operate in
268 high-multiplicity environments, such as the DUNE near detector.

269 Acknowledgments

270 We acknowledge financial support of the Swiss National Science Foundation. We would like to
271 thank Yun-Tse Tsai and Tracy L. Usher of SLAC National Accelerator Laboratory, California, USA,
272 for their valuable advice and guidance in the development of the 3D event reconstruction. We
273 would like to thank Dean Shooltz of Michigan State University, Michigan, USA, for his extensive
274 help in the design of the differential amplifiers.

275 References

- 276 [1] D. R. Nygren. ‘The Time Projection Chamber: A New 4 pi Detector for Charged Particles’.
277 In: *eConf C740805* (1974), p. 58.
- 278 [2] W. Willis and V. Radeka. ‘Liquid-argon ionization chambers as total-absorption detectors’.
279 In: *Nuclear Instruments and Methods* 120.2 (1974), pp. 221–236. ISSN: 0029-554X. DOI:
280 [https://doi.org/10.1016/0029-554X\(74\)90039-1](https://doi.org/10.1016/0029-554X(74)90039-1). URL: <http://www.sciencedirect.com/science/article/pii/0029554X74900391>.
- 282 [3] C. Rubbia. *The Liquid Argon Time Projection Chamber: A New Concept for Neutrino
283 Detectors*. Tech. rep. CERN-EP-INT-77-08. CERN, 1977.
- 284 [4] C. Rubbia et al. ‘Underground operation of the ICARUS T600 LAr-TPC: first results’. In:
285 *Journal of Instrumentation* 6.07 (2011), P07011. URL: <http://stacks.iop.org/1748-0221/6/i=07/a=P07011>.
- 287 [5] C. Anderson et al. ‘The ArgoNeuT Detector in the NuMI Low-Energy beam line at Fermilab’.
288 In: *JINST* 7 (2012), P10019. DOI: [10.1088/1748-0221/7/10/P10019](https://doi.org/10.1088/1748-0221/7/10/P10019). arXiv: [1205.6747](https://arxiv.org/abs/1205.6747)
289 [[physics.ins-det](#)].
- 290 [6] R. Acciarri et al. ‘Design and Construction of the MicroBooNE Detector’. In: *JINST*
291 12.02 (2017), P02017. DOI: [10.1088/1748-0221/12/02/P02017](https://doi.org/10.1088/1748-0221/12/02/P02017). arXiv: [1612.05824](https://arxiv.org/abs/1612.05824)
292 [[physics.ins-det](#)].
- 293 [7] J. Joshi and X. Qian. ‘Signal Processing in the MicroBooNE LArTPC’. In: (2015). arXiv:
294 [1511.00317](https://arxiv.org/abs/1511.00317) [[physics.ins-det](#)]. URL: <https://inspirehep.net/record/1402347/files/arXiv:1511.00317.pdf>.
- 296 [8] B. Rossi et al. ‘A prototype liquid Argon Time Projection Chamber for the study of UV
297 laser multi-photonic ionization’. In: *Journal of Instrumentation* 4.07 (2009), P07011. URL:
298 <http://stacks.iop.org/1748-0221/4/i=07/a=P07011>.
- 299 [9] M. Auger et al. ‘On the Electric Breakdown in Liquid Argon at Centimeter Scale’. In:
300 *JINST* 11.03 (2016), P03017. DOI: [10.1088/1748-0221/11/03/P03017](https://doi.org/10.1088/1748-0221/11/03/P03017). arXiv: [1512.05968](https://arxiv.org/abs/1512.05968)
301 [[physics.ins-det](#)].

- 302 [10] M. Auger et al. ‘A method to suppress dielectric breakdowns in liquid argon ionization
 303 detectors for cathode to ground distances of several millimeters’. In: *JINST* 9 (2014), P07023.
 304 DOI: 10.1088/1748-0221/9/07/P07023. arXiv: 1406.3929 [physics.ins-det].
- 305 [11] H. Kubo et al. ‘Development of a time projection chamber with micro pixel electrodes’. In:
 306 *Nucl. Instrum. Meth.* A513 (2003), pp. 94–98. DOI: 10.1016/j.nima.2003.08.009. arXiv:
 307 hep-ex/0301009 [hep-ex].
- 308 [12] R. Acciarri et al. ‘Long-Baseline Neutrino Facility (LBNF) and Deep Underground Neutrino
 309 Experiment (DUNE) : Conceptual Design Report, Volume 4 The DUNE Detectors at LBNF’.
 310 In: (2016). arXiv: 1601.02984 [physics.ins-det].
- 311 [13] G. D. Geronimo et al. ‘Front-End ASIC for a Liquid Argon TPC’. In: *IEEE Transactions on
 312 Nuclear Science* 58.3 (June 2011), pp. 1376–1385. ISSN: 0018-9499. DOI: 10.1109/TNS.2011.
 313 2127487.
- 314 [14] A. Krieger et al. ‘A micropower readout ASIC for pixelated liquid Ar TPCs’. In: *Topical
 315 Workshop on Electronics for Particle Physics*. 2017. URL: <https://pos.sissa.it/313>.
- 316 [15] R. Acciarri et al. ‘Long-Baseline Neutrino Facility (LBNF) and Deep Underground Neutrino
 317 Experiment (DUNE) Conceptual Design Report Volume 1: The LBNF and DUNE Projects’.
 318 In: (2016). arXiv: 1601.05471 [physics.ins-det].
- 319 [16] R. Acciarri et al. ‘Long-Baseline Neutrino Facility (LBNF) and Deep Underground Neutrino
 320 Experiment (DUNE) Conceptual Design Report Volume 2: The Physics Program for DUNE
 321 at LBNF’. In: (2016). arXiv: 1512.06148 [physics.ins-det].
- 322 [17] J. Strait et al. ‘Long-Baseline Neutrino Facility (LBNF) and Deep Underground Neutrino
 323 Experiment (DUNE) Conceptual Design Report Volume 3: Long-Baseline Neutrino Facility
 324 for DUNE’. In: (2016). arXiv: 1601.05823 [physics.ins-det].
- 325 [18] R. Sarpeshkar, T. Delbruck and C. Mead. ‘White noise in MOS transistors and resistors’. In:
 326 *IEEE Circuits and Devices Magazine* 9.6 (1993), pp. 23–29. DOI: 10.1109/101.261888.
- 327 [19] A. Ereditato et al. ‘Performance of cryogenic charge readout electronics with the ARGON-
 328 TUBE LAr TPC’. In: *JINST* 9.11 (2014), P11022. DOI: 10.1088/1748-0221/9/11/P11022.
 329 arXiv: 1408.7046 [physics.ins-det].
- 330 [20] F. Cavanna et al. ‘LArIAT: Liquid Argon In A Testbeam’. In: (2014). arXiv: 1406.5560
 331 [physics.ins-det].
- 332 [21] M. Auger. ‘New Micromegas based Readout techniques for Imaging in Time Projection
 333 Chambers’. PhD thesis. University of Bern, Switzerland, 2012.
- 334 [22] Z. Moss et al. ‘A Factor of Four Increase in Attenuation Length of Dipped Lightguides for Li-
 335 quid Argon TPCs Through Improved Coating’. In: (2016). arXiv: 1604.03103 [physics.ins-det].
- 336 [23] M. Auger et al. ‘Multi-channel front-end board for SiPM readout’. In: *JINST* 11.10 (2016),
 337 P10005. DOI: 10.1088/1748-0221/11/10/P10005. arXiv: 1606.02290 [physics.ins-det].
- 338 [24] M. Auger et al. ‘A Novel Cosmic Ray Tagger System for Liquid Argon TPC Neutrino
 339 Detectors’. In: *Instruments* 1.1 (2017), p. 2. DOI: 10.3390/instruments1010002. arXiv:
 340 1612.04614 [physics.ins-det].
- 341 [25] I. Badhrees et al. ‘Measurement of the two-photon absorption cross-section of liquid argon
 342 with a time projection chamber’. In: *New J. Phys.* 12 (2010), p. 113024. DOI: 10.1088/1367-
 343 2630/12/11/113024. arXiv: 1011.6001 [physics.ins-det].
- 344 [26] A. Blatter et al. ‘Experimental study of electric breakdowns in liquid argon at centimeter scale’.
 345 In: *JINST* 9 (2014), P04006. DOI: 10.1088/1748-0221/9/04/P04006. arXiv: 1401.6693
 346 [physics.ins-det].
- 347 [27] C. Patrignani et al. ‘Review of Particle Physics’. In: *Chinese Physics C* 40.10 (2016), p. 100001.
 348 URL: <http://stacks.iop.org/1674-1137/40/i=10/a=100001>.
- 349 [28] E. Aprile et al. *Noble Gas Detectors*. Wiley, 2008. ISBN: 9783527405978. DOI: 10.1002/
 350 9783527610020.

- 351 [29] S. Amoruso et al. ‘Study of electron recombination in liquid argon with the ICARUS TPC’. In: *Nuclear Instruments and Methods in Physics Research Section A: Accelerators, Spectrometers, Detectors and Associated Equipment* 523.3 (2004), pp. 275–286. ISSN: 0168-9002. DOI: <https://doi.org/10.1016/j.nima.2003.11.423>. URL: <http://www.sciencedirect.com/science/article/pii/S0168900204000506>.
- 356 [30] R. Acciarri et al. ‘A study of electron recombination using highly ionizing particles in the ArgoNeuT Liquid Argon TPC’. In: *Journal of Instrumentation* 8.08 (2013), P08005. URL: <http://stacks.iop.org/1748-0221/8/i=08/a=P08005>.
- 359 [31] M. Zeller et al. ‘First measurements with ARGONTUBE, a 5m long drift Liquid Argon TPC’. In: *Nuclear Instruments and Methods in Physics Research Section A: Accelerators, Spectrometers, Detectors and Associated Equipment* 718. Supplement C (2013). Proceedings of the 12th Pisa Meeting on Advanced Detectors, pp. 454–458. ISSN: 0168-9002. DOI: <https://doi.org/10.1016/j.nima.2012.11.181>. URL: <http://www.sciencedirect.com/science/article/pii/S0168900212015288>.
- 365 [32] Gushchin et al. ‘Electron dynamics in condensed argon and xenon’. In: *Journal of Experimental and Theoretical Physics* 55.4 (Apr. 1982), p. 650.
- 367 [33] V. Chepel and H. Araújo. ‘Liquid noble gas detectors for low energy particle physics’. In: *Journal of Instrumentation* 8.04 (2013), R04001. URL: <http://stacks.iop.org/1748-0221/8/i=04/a=R04001>.
- 370 [34] I. Jolliffe. *Principal Component Analysis*. Springer Series in Statistics. Springer, 2002. ISBN: 9780387954424. URL: https://books.google.ch/books?id=%5C_olByCrhjwIC.
- 372 [35] C. Höppner et al. ‘A novel generic framework for track fitting in complex detector systems’. In: *Nuclear Instruments and Methods in Physics Research Section A: Accelerators, Spectrometers, Detectors and Associated Equipment* 620.2 (2010), pp. 518–525. ISSN: 0168-9002. DOI: <https://doi.org/10.1016/j.nima.2010.03.136>. URL: <http://www.sciencedirect.com/science/article/pii/S0168900210007473>.
- 377 [36] J. Rauch and T. Schlüter. ‘GENFIT — a Generic Track-Fitting Toolkit’. In: *Journal of Physics: Conference Series* 608.1 (2015), p. 012042. URL: <http://stacks.iop.org/1742-6596/608/i=1/a=012042>.